

1

2 Modular atlases mapping strategies for diverse 3 cell type data of the mouse brain

4 Nicholas J. Tustison¹, Min Chen², Fae N. Kronman³, Jeffrey T. Duda², Clare Gamlin⁴, Mia
5 G. Tustison, Michael Kunst⁴, Rachel Dalley⁴, Staci Sorenson⁴, Quanxin Wang⁴, Lydia Ng⁴,
6 Yongsoo Kim³, and James C. Gee²

7 ¹Department of Radiology and Medical Imaging, University of Virginia, Charlottesville, VA

8 ²Department of Radiology, University of Pennsylvania, Philadelphia, PA

9 ³Department of Neural and Behavioral Sciences, Penn State University, Hershey, PA

10 ⁴Allen Institute for Brain Science, Seattle, WA

11 _____

12 Corresponding authors:

13

14 Nicholas J. Tustison, DSc

15 Department of Radiology and Medical Imaging

16 University of Virginia

17 ntustison@virginia.edu

18

19 James C. Gee, PhD

20 Department of Radiology

21 University of Pennsylvania

22 gee@upenn.edu

²³ **Abstract**

²⁴ Large-scale, international collaborative efforts by members of the BRAIN Initiative Cell Census
²⁵ Network (BICCN) consortium have recently begun aggregating the most comprehensive
²⁶ reference database to date for diverse cell type profiling of the mouse brain, which encompasses
²⁷ over 40 different multi-modal profiling techniques from more than 30 research groups. One
²⁸ central challenge for this integrative effort across different investigators and laboratories has
²⁹ been the need to map these unique datasets into common reference spaces such that the
³⁰ spatial, structural, and functional information from different cell types can be jointly analyzed
³¹ across modalities. However, significant variations in the acquisition, tissue processing, and
³² imaging techniques across data types makes mapping such diverse data a multifarious problem.
³³ Different data types exhibit unique tissue distortion and signal characteristics that precludes
³⁴ a single mapping strategy from being generally applicable across all cell type data. Diverse,
³⁵ modular, and often specialized, mapping approaches are needed to address the particular
³⁶ barriers present in each modality. This work highlights atlas mapping strategies developed
³⁷ across three separate BICCN studies using the ANTsX framework to map longitudinal
³⁸ (LSFM), spatial transcriptomic (MERFISH) and high-resolution morphology (fMOST) mouse
³⁹ brain data into the Allen Common Coordinate Framework (AllenCCFv3). We discuss both
⁴⁰ common mapping strategies that can be shared across modalities, and targeted strategies
⁴¹ driven by specific challenges from each data type. Novel contributions include velocity
⁴² flow-based approaches for mapping longitudinal trajectory in the Developmental Common
⁴³ Coordinate Framework, and automated structural morphological approaches for determining
⁴⁴ cortical parcellations. Finally, we provide general guidance and open source tools to aid
⁴⁵ investigators in this effort to tailor these strategies to address unique challenges in their data
⁴⁶ without the need to develop additional specialized software.

47 1 Introduction

48 Over the past decade there have been significant advancements in mesoscopic single-cell
49 analysis of the mouse brain. It is now possible to track single neurons in mouse brains¹,
50 observe whole brain developmental changes on a cellular level², associate brain regions
51 and tissues with their genetic composition³, and locally characterize neural connectivity⁴.

52 Much of these scientific achievements have been made possible due to breakthroughs in high
53 resolution cell profiling and imaging techniques that permit submicron, multi-modal, 3D
54 characterizations of whole mouse brains. Among these include advanced techniques such
55 as micro-optical sectioning tomography⁶, tissue clearing^{1,7}, spatial transcriptomics⁹, and
56 single-cell genomic profiling[ref], which have greatly expanded the resolution and specificity
57 of single-cell measurements in the brain.

58 Recent efforts by the National Institutes of Health's Brain Research Through Advancing
59 Innovative Neurotechnologies (BRAIN) Initiative has pushed for large-scale, international
60 collaborative efforts to utilize these advanced single cell techniques to create a comprehensive
61 reference database for high-resolution transcriptomic, epigenomic, structural and imaging
62 data of the mouse brain. This consortium of laboratories and data centers, known as the
63 BRAIN Initiative Cell Census Network (BICCN), has to date archived datasets encompassing
64 over 40 different multi-modal profiling techniques from more than 30 research groups, each
65 providing unique characterizations of distinct cell types in the brain.[ref] Several of these
66 modalities have been further developed into reference atlases to facilitate spatial alignment
67 of individual brains and different data types into a common coordinate framework (CCF),
68 thus allowing diverse single-cell information to be integrated and analyzed in tandem. The
69 most notable of these atlases is the Allen Mouse Brain Common Coordinate Framework
70 (AllenCCFv3)¹⁰, which serves as the primary target coordinate space that the majority of
71 BICCN mouse data are mapped to. Other atlases include modality specific atlases[ref] to
72 help improve mapping accuracy, and the Developmental Common Coordinate Framework
73 (DevCCF)¹¹ that includes spatiotemporal information for the developing mouse brain.

⁷⁴ 1.1 Mouse brain mapping

⁷⁵ The cross-modality associations that can be learned from mapping different cell type data into
⁷⁶ a CCF is critical for improving our understanding of the complex relationships between cellular
⁷⁷ structure, morphology, and genetics in the brain. However, finding an accurate mapping
⁷⁸ between each individual mouse brain and the CCF is a challenging and heterogeneous task.
⁷⁹ There is significant variance in the acquisition, fixation and imaging protocols across different
⁸⁰ cell type data, and different tissue processing and imaging methods can potentially introduce
⁸¹ modality specific tissue distortion and signal differences.[ref] Certain modalities can have
⁸² poor intensity correspondence with the CCF, making image alignment less robust. Studies
⁸³ targeting specific regions or cell types can lead to missing anatomical correspondences. Other
⁸⁴ considerations include artifacts such as tissue distortion, holes, bubbles, folding, tears, and
⁸⁵ missing sections in the data that need to be addressed on a per-case basis. Given the diversity
⁸⁶ of these challenges, it is unlikely any single mapping approach can be generally applicable
⁸⁷ across all cell type data. Modular, and often specialized, strategies are needed to address the
⁸⁸ unique barriers present for mapping each modality.

⁸⁹ Existing solutions to address mapping cell type data into the AllenCCFv3 falls broadly into
⁹⁰ three main categories. The first consists of integrated processing platforms that directly
⁹¹ provide mapped data to the users. These include the Allen Brain Explorer[ref] for the Allen
⁹² Reference Atlas (ARA) and associated data, the Brain Architecture Portal[ref] for combined
⁹³ ex vivo radiology and histology data, and the Image and Multi-Morphology Pipeline[ref] for
⁹⁴ high resolution morphology data. These platforms provide users online access to pre-processed,
⁹⁵ multi-modal cell type data that are already mapped to the AllenCCFv3. The platforms
⁹⁶ are designed such that the data is interactable by users through integrated visualization
⁹⁷ software that allow users to spatially manipulate and explore each dataset within the mapped
⁹⁸ space. While highly convenient for investigators who are interested in studying the specific
⁹⁹ modalities provided by these platforms, these system are limited in flexibility and general
¹⁰⁰ applicability. The mapping software and pipeline are typically developed specifically with the
¹⁰¹ data type and platform in mind, and the software are rarely openly accessible to the public.
¹⁰² Investigators will find it difficult to apply the same mapping to their own data without direct

103 collaboration with platform owners.

104 The second category are specialized approaches specifically designed for mapping one or
105 more modalities into a CCF. These approaches use combinations of manual and automated
106 processes that address specific challenges in each modality. Examples include approaches for
107 mapping magnetic resonance imaging (MRI)[ref], micro-computed tomography (microCT)[ref],
108 light-sheet fluorescence microscopy (LSFM)[ref] , for fluorescence micro-optical sectioning
109 tomography (fMOST)[ref], and volumetric imaging with synchronous on-the-fly-scan and
110 readout (ViSoR)[ref] data. As specialized approaches, these techniques tend to boast higher
111 mapping accuracy, robustness, and ease of use when ran with applicable modalities. Conversely,
112 their specialized designs often rely on base assumptions regarding the data that can make
113 them rigid and difficult to adapt for new modalities or unexpected artifacts and distortions
114 in the data. Retooling these specialize software to use with new data can require significant
115 development and validation time and engineering expertise that may not be readily available
116 for all investigators.

117 The last category are modular mapping approaches constructed using general image analysis
118 toolkits, which are software packages that include varied collections of image processing,
119 segmentation and registration tools that have been previously developed, and validated for
120 general use. Examples of such toolkits include elastix[ref], slicer3D[ref], and ANTsX[ref], which
121 have all been applied towards mapping mouse cell type data. The main challenge for using
122 these approaches is that the individual tools in the toolbox are not data type specific. Thus,
123 investigators must construct pipelines that link together a variety of tools to address data
124 specific problem, and certain tools may still require specialized input data such as landmarks
125 or annotations to operate. Investigator need to be familiar with the toolkits and supply
126 effort to build such pipelines for new data type. However, unlike previously listed specialized
127 mapping approaches, which often require additional software development to address new
128 data types, toolbox driven pipelines are easier to create, making them more accessible for
129 the general user, and individual pieces of the pipeline have already been validated for other
130 efforts. Using a general toolkit allows for modular mapping strategies that can handle a
131 wide array of different data types by piecing together distinct solutions for modality specific

¹³² problems. In this work, we highlight such mapping strategies designed using ANTsX to map
¹³³ three distinct mouse cell-type data with different characteristics into the ALLENCCFv3.

¹³⁴ 1.2 Advanced Normalization Tools (ANTsX)

¹³⁵ The Advanced Normalization Tools (ANTsX) package have been used in a number of
¹³⁶ applications for mapping mouse brain data as part of core processing steps in various
¹³⁷ workflows[ref], particularly its pairwise, intensity-based image registration capabilities and
¹³⁸ bias field correction. Historically, ANTsX development is originally based on fundamental
¹³⁹ approaches to image mapping¹²⁻¹⁴, particularly in the human brain, which has resulted
¹⁴⁰ in core contributions to the field such as the widely-used Symmetric Normalization (SyN)
¹⁴¹ algorithm¹⁵. Since its development, various independent platforms have been used to evaluate
¹⁴² ANTsX image registration capabilities in the context of different application foci which
¹⁴³ include multi-site brain MRI data¹⁶, pulmonary CT data¹⁷, and most recently, multi-modal
¹⁴⁴ brain registration in the presence of tumors¹⁸.

¹⁴⁵ Apart from its registration capabilities, ANTsX comprises additional functionality such
¹⁴⁶ as template generation¹⁹, intensity-based segmentation²⁰, preprocessing^{21,22}, deep learning
¹⁴⁷ networks²³, and other miscellaneous utilities (see Table ??). The comprehensive use of the
¹⁴⁸ toolkit has demonstrated superb performance in multiple application areas (e.g., consensus
¹⁴⁹ labeling²⁴, brain tumor segmentation²⁵, and cardiac motion estimation²⁶). Importantly,
¹⁵⁰ ANTs is built on the Insight Toolkit (ITK)²⁷ deriving benefit from the open-source community
¹⁵¹ of scientists and programmers as well as providing an important resource for algorithmic
¹⁵² development, evaluation, and improvement. We use this functionality to demonstrate recently
¹⁵³ developed frameworks for mapping fluorescence micro-optical sectioning tomography (fMOST)
¹⁵⁴ and multiplexed error-robust fluorescence *in situ* hybridization (MERFISH) image data to the
¹⁵⁵ AllenCCFv3 atlas space. In addition to standard preprocessing steps (e.g., bias correction),
¹⁵⁶ additional considerations are accommodated within the ANTsX ecosystem, such as section
¹⁵⁷ reconstruction and landmark-based alignment with corresponding processing scripts available
¹⁵⁸ at <https://github.com/dontminchenit/CCFAlignmentToolkit>.

¹⁵⁹ **1.3 Novel ANTsX-based open-source contributions**

¹⁶⁰ We introduce two novel inclusions to the ANTsX toolset that were developed as part of the
¹⁶¹ MRI mapping and analysis pipeline for the Developmental Common Coordinate Framework
¹⁶² (DevCCF). Consistent with previous ANTsX development, newly introduced capabilities
¹⁶³ introduced below are available through ANTsX (specifically, via R and Python ANTsX
¹⁶⁴ packages), and illustrated through self-contained examples in the ANTsX tutorial (<https://tinyurl.com/antsxtutorial>) with a dedicated GitHub repository specific to this work
¹⁶⁵ (<https://github.com/ntustison/ANTsXMouseBrainMapping>).
¹⁶⁶

¹⁶⁷ **1.3.1 The DevCCF velocity flow model**

¹⁶⁸ Recently, the Developmental Common Coordinate Framework (DevCCF) was introduced to
¹⁶⁹ the mouse brain research community as a public resource¹¹ comprising symmetric atlases of
¹⁷⁰ multimodal image data and anatomical segmentations defined by developmental ontology.
¹⁷¹ These templates sample the mouse embryonic days (E) 11.5, E13.5, E15.5, E18.5 and postnatal
¹⁷² day (P) 4, P14, and P56. Modalities include light sheet florescence microscopy (LSFM)
¹⁷³ and at least four MRI contrasts per developmental stage. Anatomical parcellations are
¹⁷⁴ also available for each time point and were generated from ANTsX-based mappings of gene
¹⁷⁵ expression and other cell type data. Additionally, the P56 template was integrated with
¹⁷⁶ the AllenCCFv3 to further enhance the practical utility of the DevCCF. These processes,
¹⁷⁷ specifically template generation and multi-modal image mapping, were performed using
¹⁷⁸ ANTsX functionality in the presence of image mapping difficulties such as missing data and
¹⁷⁹ tissue distortion.¹¹

¹⁸⁰ Given the temporal gaps in the discrete set of developmental atlases, we also provide an
¹⁸¹ open-source framework for inferring correspondence within the temporally continuous domain
¹⁸² sampled by the existing set of embryonic and postnatal atlases of the DevCCF. This recently
¹⁸³ developed functionality permits the generation of a diffeomorphic velocity flow transformation
¹⁸⁴ model²⁸, influenced by previous work²⁹. The resulting time-parameterized velocity field spans
¹⁸⁵ the stages of the DevCCF where mappings between any two continuous time points within
¹⁸⁶ the span bounded by the E11.5 and P56 atlases is determined by integration of the optimized

187 velocity field.

188 1.3.2 Structural morphology and parcellations of the mouse brain

189 In contrast to the pipeline development in human data²³, no current ANTsX tools exist yet
190 to create adequate training data for automated parcellations of the mouse brain. In addition,
191 mouse brain data acquisition often has unique issues, such as lower data quality or sampling
192 anisotropy which limits its applicability to high resolution resources (e.g., AllenCCFv3,
193 DevCCF), specifically with respect to the corresponding granular brain parcellations derived
194 from numerous hours of expert annotation leveraging multimodal imaging resources.

195 Herein, we introduce a mouse brain parcellation pipeline for T2-weighted (T2-w) MRI
196 comprising two novel deep learning components: two-shot learning brain extraction from data
197 augmentation of two ANTsX templates generated from two open datasets^{30,31} and single-shot
198 brain parcellation derived from the AllenCCFv3 labelings mapped to the corresponding
199 DevCCF P56 T2-w component. Although we anticipate that this pipeline will be beneficial
200 to the research community, this work demonstrates more generally how one can leverage
201 ANTsX tools for developing tailored brain parcellation schemes using publicly available
202 resources. Evaluation is performed on an independent open dataset³² comprising longitudinal
203 acquisitions of multiple specimens.

204 **2 Results**

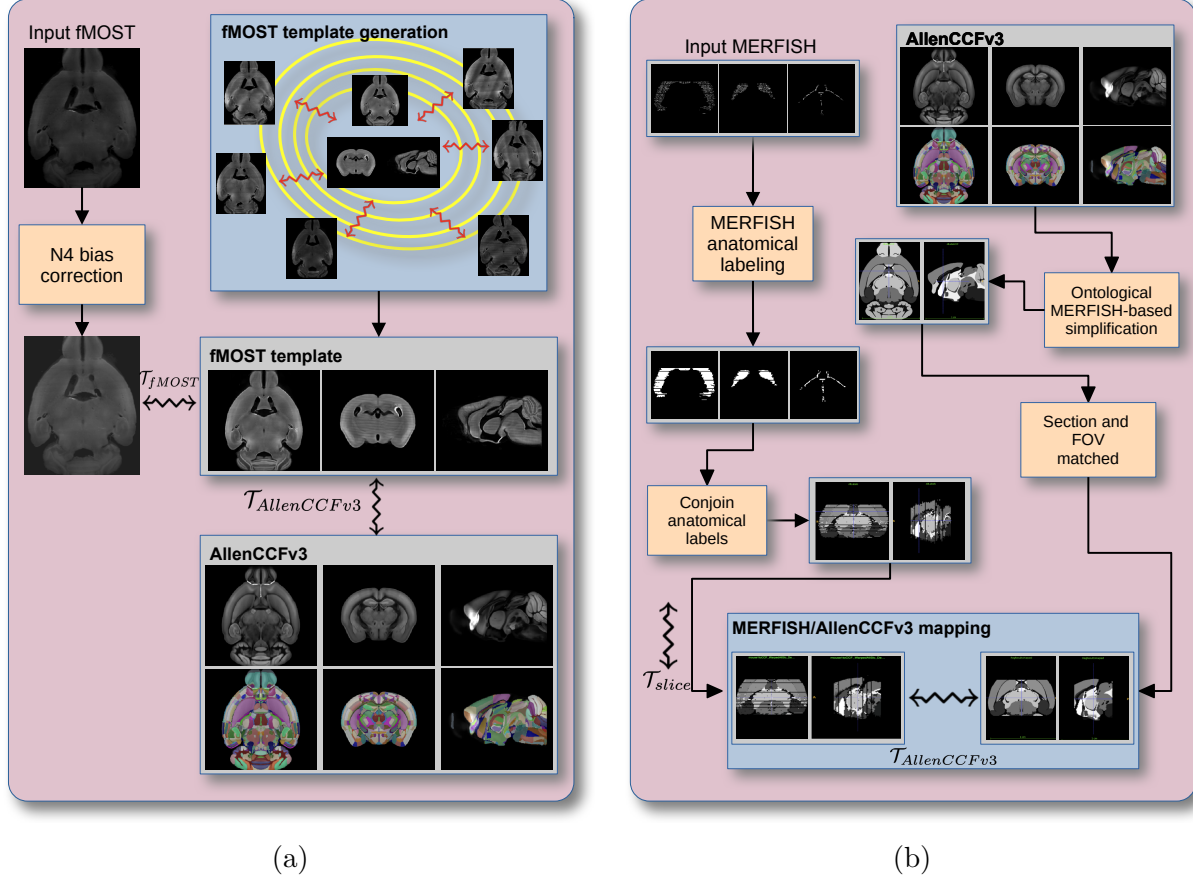


Figure 1: Diagrammatic illustration of the two ANTsX-based pipelines for mapping (a) fMOST and (b) MERFISH data into the space of AllenCCFv3. Each generates the requisite transforms, \mathcal{T} , to map individual images.

205 **2.1 AllenCCFv3 brain image mapping**

206 **2.1.1 Mapping fluorescence micro-optical sectioning tomography (fMOST) data**

207 **Overview.** A framework for mapping fluorescence micro-optical sectioning tomography
 208 (fMOST) mouse brain images into the AllenCCFv3 was developed (see Figure 1(a)). An
 209 intensity- and shape-based average fMOST atlas serves as an intermediate registration target
 210 for mapping fMOST images from individual specimens into the AllenCCFv3. Preprocessing
 211 steps include downsampling to match the $25\mu m$ isotropic AllenCCFv3, acquisition-based
 212 stripe artifact removal, and inhomogeneity correction²². Preprocessing also includes a single

annotation-driven registration to establish a canonical mapping between the fMOST atlas and the AllenCCFv3. This step allows us to align expert determined landmarks to accurately map structures with large morphological differences between the modalities, which are difficult to address using standard approaches. Once this canonical mapping is established, standard intensity-based registration is used to align each new fMOST image to the fMOST specific atlas. This mapping is concatenated with the canonical fMOST atlas-to-AllenCCFv3 mapping to further map each individual brain into the latter without the need to generate additional landmarks. Transformations learned through this mapping can be applied to single neuron reconstructions from the fMOST images to evaluate neuronal distributions across different specimens into the AllenCCFv3 for the purpose of cell census analyses.

Data. The high-throughput and high-resolution fluorescence micro-optical sectioning tomography (fMOST)^{33,34} platform was used to image 55 mouse brains containing gene-defined neuron populations, with sparse transgenic expression^{35,36}. In short, the fMOST imaging platform results in 3-D images with voxel sizes of $0.35 \times 0.35 \times 1.0\mu\text{m}^3$ and is a two-channel imaging system where the green channel displays the green fluorescent protein (GFP) labeled neuron morphology and the red channel is used to visualize the counterstained propidium iodide cytoarchitecture. The spatial normalizations described in this work were performed using the red channel, which offered higher tissue contrast for alignment, although other approaches are possible including multi-channel registration.

Evaluation. Evaluation of the canonical fMOST atlas to Allen CCFv3 mapping was performed via quantitative comparison at each step of the registration and qualitative assessment of structural correspondence after alignment by an expert anatomist. Dice values were generated for the following structures: whole brain, 0.99; fimbria, 0.91; habenular commissure, 0.63; posterior choroid plexus, 0.93; anterior choroid plexus, 0.96; optic chiasm, 0.77; caudate putamen, 0.97. Similar qualitative assessment was performed for each fMOST specimen including the corresponding neuron reconstruction data.

239 **2.1.2 Mapping multiplexed error-robust fluorescence in situ hybridization**
240 **(MERFISH) data**

241 **Overview.** The unique aspects of mapping multiplexed error-robust fluorescence in situ
242 hybridization (MERFISH) spatial transcriptomic data onto AllenCCFv3³⁷ required the
243 development of a separate ANTsX-based pipeline (see Figure 1(b)). Mappings are performed
244 by matching gene expression derived region labels from the MERFISH data to corresponding
245 anatomical parcellations of the AllenCCFv3. The pipeline consists of MERFISH data specific
246 preprocessing which includes section reconstruction, mapping corresponding anatomical
247 labels between AllenCCFv3 and the spatial transcriptomic maps of the MERFISH data,
248 and matching MERFISH sections to the atlas space. Following pre-processing, two main
249 alignment steps were performed: 1) 3-D global affine mapping and section matching of the
250 AllenCCFv3 into the MERFISH data and 2) 2D global and deformable mapping between each
251 MERFISH section and matched AllenCCFv3 section. Mappings learned via each step in the
252 pipeline are preserved and concatenated to provide point-to-point correspondence between
253 the original MERFISH data and AllenCCFv3, thus allowing individual gene expressions to
254 be transferred into the AllenCCFv3.

255 **Data.** MERFISH mouse brain data was acquired using a previously detailed procedure³⁷.
256 Briefly, a brain of C57BL/6 mouse was dissected according to standard procedures and placed
257 into an optimal cutting temperature (OCT) compound (Sakura FineTek 4583) in which it
258 was stored at -80°C. The fresh frozen brain was sectioned at 10 μ m on Leica 3050 S cryostats
259 at intervals of 200 μ m to evenly cover the brain. A set of 500 genes were imaged that had
260 been carefully chosen to distinguish the ~ 5200 clusters of our existing RNAseq taxonomy.
261 For staining the tissue with MERFISH probes, a modified version of instructions provided by
262 the manufacturer was used³⁷. Raw MERSCOPE data were decoded using Vizgen software
263 (v231). Cell segmentation was performed³⁸. In brief, cells were segmented based on DAPI
264 and PolyT staining using Cellpose³⁹. Segmentation was performed on a median z-plane
265 (fourth out of seven) and cell borders were propagated to z-planes above and below. To assign
266 cluster identity to each cell in the MERFISH dataset, we mapped the MERFISH cells to the
267 scRNA-seq reference taxonomy.

268 **Evaluation.** Alignment of the MERFISH data into the AllenCCFv3 was qualitatively assessed
 269 by an expert anatomist at each iteration of the registration using known correspondence of
 270 gene markers and their associations with the AllenCCFv3. As previously reported³⁷, further
 271 assessment of the alignment showed that, of the 554 terminal regions (gray matter only)
 272 in the AllenCCFv3, only seven small subregions were missed from the MERFISH dataset:
 273 frontal pole, layer 1 (FRP1), FRP2/3, FRP5; accessory olfactory bulb, glomerular layer
 274 (AOBgl); accessory olfactory bulb, granular layer (AOBgr); accessory olfactory bulb, mitral
 275 layer (AOBmi); and accessory supraoptic group (ASO).

276 **2.2 The DevCCF velocity flow model**

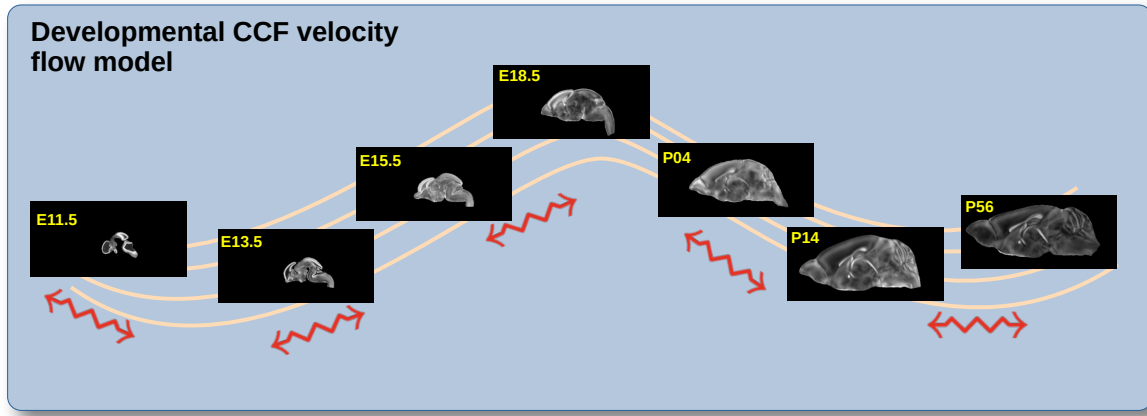


Figure 2: The spatial transformation between any two time points within the DevCCF longitudinal developmental trajectory is available through the use of ANTsX functionality for generating a velocity flow model.

277 To continuously interpolate transformations between the different stages of the DevCCF
 278 atlases, a velocity flow model was constructed using DevCCF derived data and functionality
 279 recently introduced into both the ANTsR and ANTsPy packages. Both platforms include
 280 a complete suite of functions for determining dense correspondence from sparse landmarks
 281 based on a variety of transformation models ranging from standard linear models (i.e., rigid,
 282 affine) to deformable diffeomorphic models (e.g, symmetric normalization¹⁵). The latter set
 283 includes transformation models for both the pairwise scenario and for multiple sets, as in the
 284 case of the DevCCF. ANTsX, being built on top of ITK, uses an ITK image data structure

285 for the 4-D velocity field where each voxel contains the x , y , z components of the field at
286 that point.

287 **2.2.1 Data**

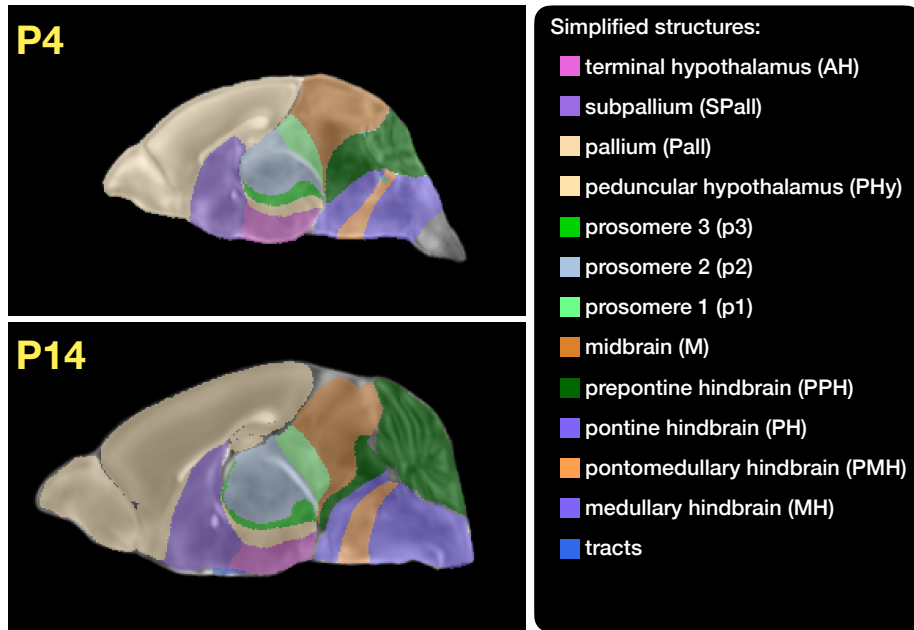


Figure 3: Annotated regions representing common labels across developmental stages which are illustrated for both P4 and P14.

288 Labeled annotations are available as part of the original DevCCF and reside in the space
289 of each developmental template which range in resolution from $31.5 - 50\mu\text{m}$. Across all
290 atlases, the total number of labeled regions exceeds 2500. From these labels, a common set
291 of 26 labels (13 per hemisphere) across all atlases were used for optimization and evaluation.
292 These simplified regions include: terminal hypothalamus, subpallium, pallium, peduncular
293 hypothalamus, prosomere, prosomere, prosomere, midbrain, prepontine hindbrain, pontine
294 hindbrain, pontomedullary hindbrain, medullary hindbrain, and tracts (see Figure 3).

295 Prior to velocity field optimization, all data were rigidly transformed to DevCCF P56 using
296 the centroids of the common label sets. In order to determine the landmark correspondence
297 across DevCCF stages, the multi-metric capabilities of `ants.registration(...)` were used.
298 Instead of performing intensity-based pairwise registration directly on these multi-label
299 images, each label was used to construct a separate fixed and moving image pair resulting in

300 a multi-metric registration optimization scenario involving 24 binary image pairs (each label
 301 weighted equally) for optimizing diffeomorphic correspondence between neighboring time
 302 point atlases using the mean squares metric and the symmetric normalization transform¹⁵.
 303 To generate the set of common point sets across all seven developmental atlases, the label
 304 boundaries and whole regions were sampled in the P56 atlas and then propagated to each atlas
 305 using the transformations derived from the pairwise registrations. We selected a sampling
 306 rate of 10% for the contour points and 1% for the regional points for a total number of points
 307 being per atlas being 173303 ($N_{contour} = 98151$ and $N_{region} = 75152$). Regional boundary
 308 points were weighted twice as those of non-boundary points during optimization.

309 2.2.2 Optimization

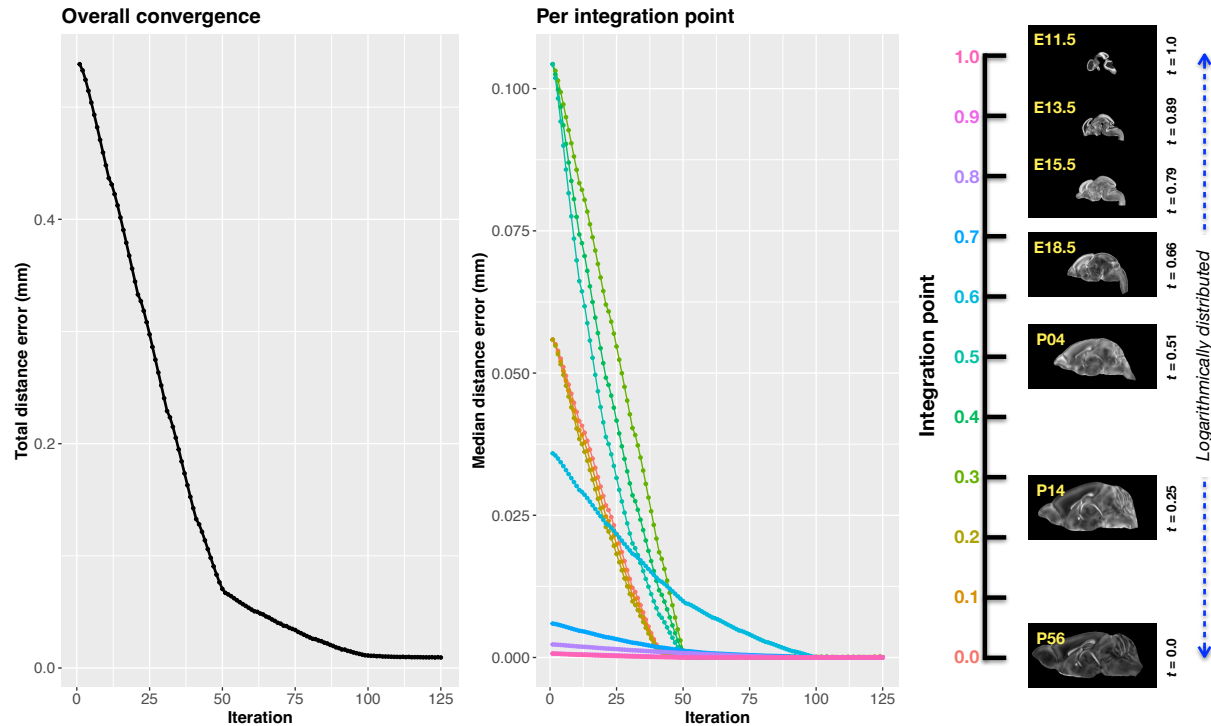


Figure 4: Convergence of the optimization of the velocity field for describing the transformation through the developmental stages from E11.5 through P56. Integration points in diagram on the right are color-coordinated with the center plot and placed in relation to the logarithmically situated temporal placement of the individual DevCCF atlases.

310 The velocity field was optimized using the input composed of the seven corresponding point
 311 sets and their associated weight values, the selected number of integration points for the

312 velocity field ($N = 11$), and the parameters defining the geometry of the spatial dimensions
313 of the velocity field. Thus, the optimized velocity field described here is of size [256, 182, 360]
314 (50 μ m isotropic) $\times 11$ integration points for a total compressed size of a little over 2 GB.
315 This choice represented weighing the trade-off between tractability, portability, and accuracy.
316 However, all data and code to reproduce the results described (with possible variation in the
317 input parameters) are available in the dedicated GitHub repository.

318 The normalized time point scalar value for each atlas/point-set in the temporal domains [0, 1]
319 was also defined. Given the increasingly larger gaps in the postnatal timepoint sampling, we
320 made two adjustments. Based on known mouse brain development, we used 28 days for the
321 P56 data. We then computed the log transform of the adjusted set of time points prior to
322 normalization between 0 and 1 (see the right side of Figure 4). This log transform, as part of
323 the temporal normalization, significantly improved data spacing.

324 The maximum number of iterations was set to 200 with each iteration taking approximately
325 six minutes on a 2020 iMac (processor, 3.6 GHz 10-Core Intel Core i9; memory, 64 GB 2667
326 MHz DDR4) At each iteration we looped over the 11 integration points. At each integration
327 point, the velocity field estimate was updated by warping the two immediately adjacent
328 point sets to the integration time point and determining the regularized displacement field
329 between the two warped point sets. As with any gradient-based descent algorithm, this
330 field was multiplied by a small step size ($\delta = 0.2$) before adding to the current velocity field.
331 Convergence is determined by the average displacement error over each of the integration
332 points. As can be seen in the left panel of Figure 4, convergence occurred around 125
333 iterations when the average displacement error over all integration points is minimized. The
334 median displacement error at each of the integration points also trends towards zero but at
335 different rates.

336 2.2.3 The transformation model

337 Once optimized, the resulting velocity field can be used to generate the deformable transform
338 between any two continuous points within the time interval bounded by E11.5 and P56.
339 In Figure 5, we transform each atlas to the space of every other atlas using the DevCCF

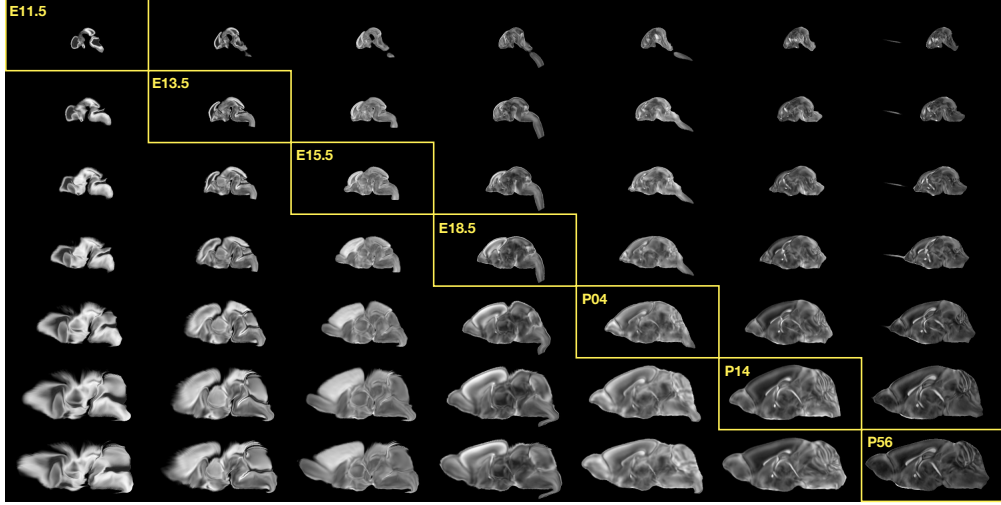


Figure 5: Mid-sagittal visualization of the effects of the transformation model in warping every developmental stage to the time point of every other developmental stage. The original images are located along the diagonal. Columns correspond to the warped original image whereas the rows represent the reference space to which each image is warped.

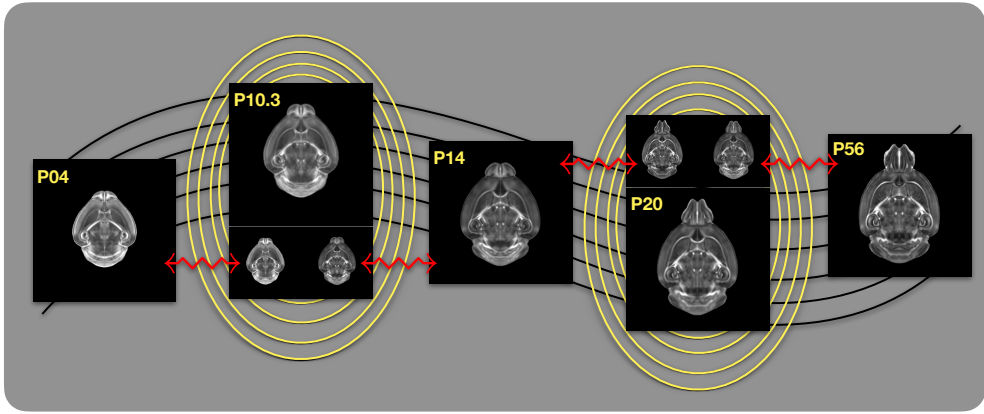


Figure 6: Illustration of the use of the velocity flow model for creating virtual templates at continuous time points not represented in one of the existing DevCCF time points. For example, FA templates at time point P10.3 and P20 can be generated by warping the existing temporally adjacent developmental templates to the target time point and using those images in the ANTsX template building process.

transform model. Additionally, one can use this transformation model to construct virtual templates in the temporal gaps of the DevCCF. Given an arbitrarily chosen time point within the normalized time point interval, the existing adjacent DevCCF atlases on either chronological side can be warped to the desired time point. A subsequent call to one of the ANTsX template building functions then permits the construction of the template at

345 that time point. In Figure 6, we illustrate the use of the DevCCF velocity flow model for
 346 generating two such virtual templates for two arbitrary time points. Note that both of these
 347 usage examples can be found in the GitHub repository previously given.

348 2.3 The Mouse Brain Parcellation Pipeline

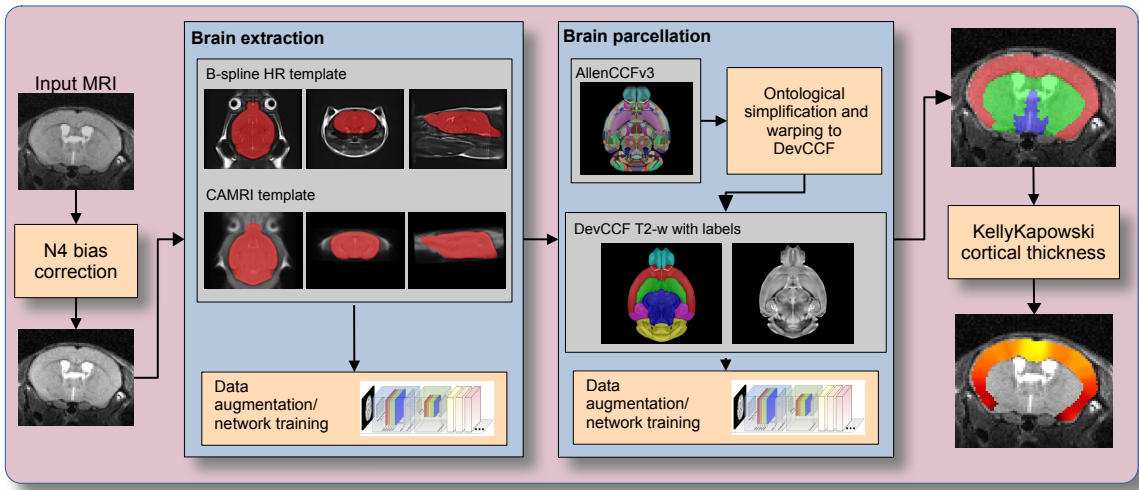


Figure 7: The mouse brain cortical parcellation pipeline integrating two deep learning components for brain extraction and brain parcellation prior to estimating cortical labels. Both deep learning networks rely heavily on data augmentation on templates built from open data and provide an outline for further refinement and creating alternative parcellations for tailored research objectives.

349 One of the most well-utilized pipelines in the ANTsX toolkit is the generation of cortical
 350 thickness maps in the human brain from T1-weighted MRI. Starting with the novel Diffeomor-
 351 phic Registration-based Cortical Thickness (DiReCT) algorithm⁴⁰, a complete algorithmic
 352 workflow was developed for both cross-sectional⁴¹ and longitudinal⁴² T1-weighted MR image
 353 data. This contribution was later refactored using deep learning²³ leveraging the earlier
 354 results⁴¹ for training data.

355 In the case of the mouse brain, the lack of training data and/or tools to generate training
 356 data making analogous algorithmic development difficult. In addition, mouse data is often
 357 characterized by unique issues such as frequent anisotropic sampling which are often in sharp
 358 contrast to the high resolution resources available within the community, e.g., AllenCCFv3
 359 and DevCCF. Using ANTsX and other publicly available data resources, we developed a

360 complete mouse brain structural morphology pipeline as illustrated in Figure 7 and detailed
361 below.

362 **2.3.1 Two-shot mouse brain extraction network**

363 In order to create a generalized mouse brain extraction network, we built whole-head templates
364 from two publicly available datasets. The Center for Animal MRI (CAMRI) dataset³⁰ from
365 the University of North Carolina at Chapel Hill consists of 16 T2-weighted MRI volumes
366 of voxel resolution $0.16 \times 0.16 \times 0.16 mm^3$. The second high-resolution dataset³¹ comprises
367 88 specimens each with three spatially aligned canonical views with in-plane resolution of
368 $0.08 \times 0.08 mm^2$ with a slice thickness of $0.5 mm$. These three orthogonal views were used
369 to reconstruct a single high-resolution volume per subject using a B-spline fitting algorithm
370 developed in ANTsX⁴³. From these two datasets, two symmetric isotropic ANTsX templates¹⁹
371 were generated analogous to the publicly available ANTsX human brain templates used in
372 previous research⁴¹. Bias field simulation, intensity histogram warping, noise simulation,
373 random translation and warping, and random anisotropic resampling in the three canonical
374 directions were used for data augmentation in training a T2-weighted brain extraction
375 network.

376 **2.3.2 Single-shot mouse brain parcellation network**

377 To create the network for generating a brain parcellation consistent with cortical thickness
378 estimation, we used the AllenCCFv3 and the associated `allensdk` Python library. Using
379 `allensdk`, a gross parcellation labeling was generated from the fine Allen CCFv3 labeling
380 which includes the cerebral cortex, cerebral nuclei, brain stem, cerebellum, main olfactory
381 bulb, and hippocampal formation. This labeling was mapped to the P56 component of
382 the DevCCF. Both the T2-w P56 DevCCF and labelings, in conjunction with the data
383 augmentation described previously for brain extraction, was used to train a brain parcellation
384 network.

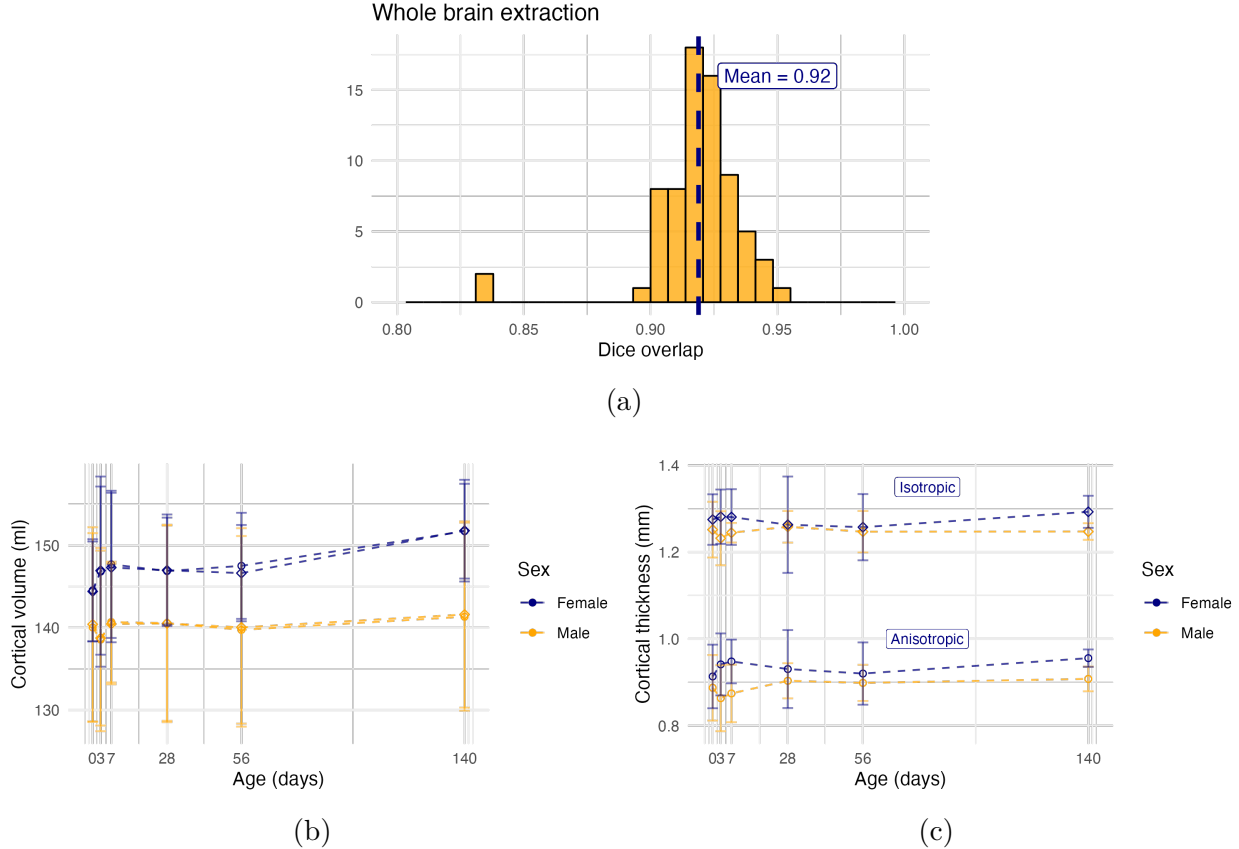


Figure 8: Evaluation of the ANTsX mouse brain extraction, parcellation, and cortical thickness pipeline on an independent dataset consisting of 12 specimens \times 7 time points = 84 total images. (a) Dice overlap comparisons with the provided brain masks provide generally good agreement with the brain extraction network. (b) Cortical volume measurements show similar average quantities over growth and development between the original anisotropic data and interpolated isotropic data. (c) These results contrast with the cortical thickness measurements which show that cortical thickness estimation in anisotropic space severely underestimates the actual values.

³⁸⁵ **2.3.3 Evaluation**

³⁸⁶ For evaluation, we used an additional publicly available dataset³² which is completely
³⁸⁷ independent from the data used in training the brain extraction and parcellation networks.
³⁸⁸ Data includes 12 specimens each imaged at seven time points (Day 0, Day 3, Week 1, Week
³⁸⁹ 4, Week 8, Week 20) with available brain masks. In-plane resolution is $0.1 \times 0.1mm^2$ with a
³⁹⁰ slice thickness of $0.5mm$. Since the training data is isotropic and data augmentation includes
³⁹¹ downsampling in the canonical directions, each of the two networks learns mouse brain-specific
³⁹² interpolation such that one can perform prediction on thick-sliced images, as, for example, in
³⁹³ these evaluation data, and return isotropic probability and thickness maps (a choice available
³⁹⁴ to the user). Figure 8 summarizes the results of the evaluation and comparison between
³⁹⁵ isotropic and anisotropic cortical measurements in male and female specimens.

³⁹⁶ **3 Discussion**

³⁹⁷ The ANTsX ecosystem is a powerful framework that has demonstrated applicability to
³⁹⁸ multiple species and organ systems, including the mouse brain. This is further evidenced by
³⁹⁹ the many software packages that use various ANTsX components in their own mouse-specific
⁴⁰⁰ workflows. In and of itself, the extensive functionality of ANTsX makes it possible to create
⁴⁰¹ complete processing pipelines without requiring the integration of multiple packages. These
⁴⁰² open-source components not only perform well but are available across multiple platforms
⁴⁰³ which facilitates the construction of tailored pipelines for individual study solutions. These
⁴⁰⁴ components are also supported by years of development not only by the ANTsX development
⁴⁰⁵ team but by the larger ITK community.

⁴⁰⁶ In the case of the development of the DevCCF, ANTsX was crucial in providing neces-
⁴⁰⁷ sary functionality for yielding high quality output. For the generation of the individual
⁴⁰⁸ developmental stage multi-modal, symmetric templates, ANTsX is unique amongst image
⁴⁰⁹ analysis software packages in providing existing solutions for template generation which have
⁴¹⁰ been thoroughly vetted, including being used in several studies over the years, and which
⁴¹¹ continue to be under active refinement. At its core, computationally efficient and quality
⁴¹² template generation requires the use of precision pairwise image mapping functionality which,
⁴¹³ historically, is at the origins of the ANTsX ecosystem. Moreover, these mapping capabilities
⁴¹⁴ extend beyond template generation to the mapping of other image data (e.g., gene expression
⁴¹⁵ maps) to a selected template for providing further insight into the mouse brain.

⁴¹⁶ With respect to the DevCCF, despite the significant expansion of available developmental age
⁴¹⁷ templates beyond what existed previously, there are still temporal gaps in the DevCCF which
⁴¹⁸ can be potentially sampled by future research efforts. However, pioneering work involving
⁴¹⁹ time-varying diffeomorphic transformations allow us to continuously situate the existing
⁴²⁰ templates within a velocity flow model. This allows one to determine the diffeomorphic
⁴²¹ transformation from any one temporal location to any other temporal location within the time
⁴²² span defined by the temporal limits of the DevCCF. This functionality is built on multiple
⁴²³ ITK components including the B-spline scattered data approximation technique for field
⁴²⁴ regularization and velocity field integration. This velocity field model permits intra-template

425 comparison and the construction of virtual templates where a template can be estimated at
426 any continuous time point within the temporal domain. This novel application can potentially
427 enhance our understanding of intermediate developmental stages.

428 We also presented a mouse brain pipeline for brain extraction, parcellation, and cortical
429 thickness using single-shot and two-shot learning with data augmentation. This approach
430 attempts to circumvent (or at least minimize) the typical requirement of large training
431 datasets as with the human ANTsX pipeline analog. However, even given our initial success
432 on independent data, we fully anticipate that refinements will be necessary. Given that the
433 ANTsX toolkit is a dynamic effort undergoing continual improvement, we manually correct
434 cases that fail and use them for future training and refinement of network weights as we have
435 done for our human-based networks. Generally, these approaches provide a way to bootstrap
436 training data for manual refinement and future generation of more accurate deep learning
437 networks in the absence of other applicable tools.

438 **4 Methods**

439 The following methods are all available as part of the ANTsX ecosystem with analogous
440 elements existing in both ANTsR (ANTs in R) and ANTsPy (ANTs in Python) with an
441 ANTs/ITK C++ core. However, most of the development for the work described below was
442 performed using ANTsPy. For equivalent calls in ANTsR, please see the ANTsX tutorial at
443 <https://tinyurl.com/antsxtutorial>.

444 **4.1 General ANTsX utilities**

445 **4.1.1 Preprocessing: bias field correction and denoising**

446 Bias field correction and image denoising are standard preprocessing steps in improving
447 overall image quality in mouse brain images. The bias field, a gradual spatial intensity
448 variation in images, can arise from various sources such as magnetic field inhomogeneity or
449 acquisition artifacts, leading to distortions that can compromise the quality of brain images.
450 Correcting for bias fields ensures a more uniform and consistent representation of brain
451 structures, enabling more accurate quantitative analysis. Additionally, brain images are
452 often susceptible to various forms of noise, which can obscure subtle features and affect the
453 precision of measurements. Denoising techniques help mitigate the impact of noise, enhancing
454 the signal-to-noise ratio and improving the overall image quality. The well-known N4 bias
455 field correction algorithm²² has its origins in the ANTs toolkit which was implemented and
456 introduced into the ITK toolkit, i.e. `ants.n4_bias_field_correction(...)`. Similarly,
457 ANTsX contains an implementation of a well-performing patch-based denoising technique²¹
458 and is also available as an image filter to the ITK community, `ants.denoise_image(...)`.

459 **4.1.2 Image registration**

460 The ANTs registration toolkit is a complex framework permitting highly tailored solutions
461 to pairwise image registration scenarios⁴⁴. It includes innovative transformation models
462 for biological modeling^{15,29} and has proven capable of excellent performance^{16,45}. Vari-
463 ous parameter sets targeting specific applications have been packaged with the different
464 ANTsX packages, specifically ANTs, ANTsPy, and ANTsR²³. In ANTsPy, the function

`ants.registration(...)` is used to register a pair of images or a pair of image sets where `type_of_transform` is a user-specified option that invokes a specific parameter set. For example `type_of_transform='antsRegistrationSyNQuick[s]'` encapsulates an oft-used parameter set for quick registration whereas `type_of_transform='antsRegistrationSyN[s]'` is a more detailed alternative. Transforming images using the derived transforms is performed via the `ants.apply_transforms(...)` function.

Initially, linear optimization is initialized with center of (intensity) mass alignment typically followed by optimization of both rigid and affine transforms using the mutual information similarity metric. This is followed by diffeomorphic deformable alignment using symmetric normalization (SyN) with Gaussian¹⁵ or B-spline regularization²⁹ where the forward transform is invertible and differentiable. The similarity metric employed at this latter stage is typically either neighborhood cross-correlation or mutual information. Note that these parameter sets are robust to input image type (e.g., light sheet fluorescence microscopy, Nissl staining, and the various MRI modalities) and are adaptable to mouse image geometry and scaling.

Further details can be found in the various documentation sources for these ANTsX packages.

4.1.3 Template generation

ANTsX provides functionality for constructing templates from a set (or multi-modal sets) of input images as originally described¹⁹ and recently used to create the DevCCF templates¹¹. An initial template estimate is constructed from an existing subject image or a voxelwise average derived from a rigid pre-alignment of the image population. Pairwise registration between each subject and the current template estimate is performed using the Symmetric Normalization (SyN) algorithm¹⁵. The template estimate is updated by warping all subjects to the space of the template, performing a voxelwise average, and then performing a “shape update” of this latter image by warping it by the average inverse deformation, thus yielding a mean image of the population in terms of both intensity and shape. The corresponding ANTsPy function is `ants.build_template(...)`.

491 **4.1.4 Visualization**

492 To complement the well-known visualization capabilities of R and Python, e.g., `ggplot2`
493 and `matplotlib`, respectively, image-specific visualization capabilities are available in the
494 `ants.plot(...)` function (Python). These are capable of illustrating multiple slices in
495 different orientations with other image overlays and label images.

496 **4.2 Mapping fMOST data to AllenCCFv3**

497 **4.2.1 Preprocessing**

- *Downsampling.* The first challenge when mapping fMOST images into the AllenCCFv3 is addressing the resolution scale of the data. Native fMOST data from an individual specimen can range in the order of terabytes, which leads to two main problems. First, volumetric registration methods (particularly those estimating local deformation) have high computational complexity and typically cannot operate on such high-resolution data under reasonable memory and runtime constraints. Second, the resolution of the AllenCCFv3 atlas is much lower than the fMOST data, thus the mapping process will cause much of the high-resolution information in the fMOST images to be lost regardless. Thus, we perform a cubic B-spline downsampling of the fMOST data to reduce the resolution of each image to match the isotropic $25 \mu\text{m}$ voxel resolution of the AllenCCFv3 intensity atlas using `ants.resample_image(...)`. An important detail to note is that while the fMOST images and atlas are downsampled, the mapping learned during the registration is assumed to be continuous. Thus, after establishing the mapping to the AllenCCFv3, we can interpolate the learned mapping and apply it directly to the high-resolution native data directly to transform any spatially aligned data (such as the single-cell neuron reconstructions) into the AllenCCFv3.
- *Stripe artifact removal.* Repetitive pattern artifacts are a common challenge in fMOST imaging where inhomogeneity during the cutting and imaging of different sections can leave stripes of hyper- and hypo-intensity across the image. These stripe artifacts can be latched onto by the registration algorithm as unintended features that are

518 then misregistered to non-analogous structures in the AllenCCFv3. We address these
519 artifacts by fitting a 3-D bandstop (notch) filter to target the frequency of the stripe
520 patterns and removing them prior to the image registration.

- 521 • *Inhomogeneity correction.* Regional intensity inhomogeneity can also occur within
522 and between sections in fMOST imaging due to staining or lighting irregularity during
523 acquisition. Similar to stripe artifacts, intensity gradients due to inhomogeneity
524 can be misconstrued as features during the mapping and result in matching of non-
525 corresponding structures. Our pipeline addresses these intensity inhomogeneities using
526 N4 bias field correction²², `ants.n4_bias_field_correction(...)`.

527 **4.2.2 Steps for spatial normalization to AllenCCFv3**

528 1. *Average fMOST atlas as an intermediate target.* Due to the preparation of the mouse
529 brain for fMOST imaging, the resulting structure in the mouse brain has several large
530 morphological deviations from the AllenCCFv3 atlas. Most notable of these is an
531 enlargement of the ventricles, and compression of cortical structures. In addition,
532 there is poor intensity correspondence for the same anatomic features due to intensity
533 dissimilarity between imaging modalities. We have found that standard intensity-base
534 registration is insufficient to capture the significant deformations required to map these
535 structures correctly into the AllenCCFv3. We address this challenge in ANTsX by using
536 explicitly corresponding parcellations of the brain, ventricles and surrounding structures
537 to directly recover these large morphological differences. However, generating these
538 parcellations for each individual mouse brain is a labor-intensive task. Our solution
539 is to create an average atlas whose mapping to AllenCCFv3 encapsulates these large
540 morphological differences to serve as an intermediate registration point. This has the
541 advantage of only needing to generate one set of corresponding annotations which is
542 used to register between the two atlas spaces. New images are first aligned to the
543 fMOST average atlas, which shares common intensity and morphological features and
544 thus can be achieved through standard intensity-based registration.

545 2. *Average fMOST atlas construction.* An intensity and shape-based contralaterally

546 symmetric average of the fMOST image data is constructed from 30 images and their
547 contralateral flipped versions. We ran three iterations of the atlas construction using the
548 default settings. Additional iterations (up to six) were evaluated and showed minimal
549 changes to the final atlas construction, suggesting a convergence of the algorithm.

- 550 3. *fMOST atlas to AllenCCFv3 alignment.* Alignment between the fMOST average atlas
551 and AllenCCFv3 was performed using a one-time annotation-driven approach. Label-
552 to-label registration is used to align 7 corresponding annotations in both atlases in the
553 following: 1) brain mask/ventricles, 2) caudate/putamen, 3) fimbria, 4) posterior choroid
554 plexus, 5) optic chiasm, 6) anterior choroid plexus, and 7) habenular commissure. The
555 alignments were performed sequentially, with the largest, most relevant structures being
556 aligned first using coarse registration parameters, followed by other structures using
557 finer parameters. This coarse-to-fine approach allows us to address large morphological
558 differences (such as brain shape and ventricle expansion) at the start of registration
559 and then progressively refine the mapping using the smaller structures. The overall
560 ordering of these structures was determined manually by an expert anatomist, where
561 anatomical misregistration after each step of the registration was evaluated and used to
562 determine which structure should be used in the subsequent iteration to best improve
563 the alignment. The transformation from this one-time expert-guided alignment is
564 preserved and used as the canonical fMOST atlas to AllenCCFv3 mapping in the
565 pipeline.
- 566 4. *Alignment of individual fMOST mouse brains.* The canonical transformation between
567 the fMOST atlas and AllenCCFv3 greatly simplifies the registration of new individual
568 fMOST mouse brains into the AllenCCFv3. Each new image is first registered into the
569 fMOST average atlas, which shares intensity, modality, and morphological characteris-
570 tics. This allows us to leverage standard, intensity-based registration functionality⁴⁴
571 available in ANTsX to perform this alignment. Transformations are then concate-
572 nated to the original fMOST image to move it into the AllenCCFv3 space using
573 `ants.apply_transforms(...)`.
- 574 5. *Transformation of single cell neurons.* A key feature of fMOST imaging is the ability

575 to reconstruct and examine whole-brain single neuron projections³⁶. Spatial mapping
576 of these neurons from individual brains into the AllenCCFv3 allows investigators to
577 study different neuron types within the same space and characterize their morphology
578 with respect to their transcriptomics. Mappings found between the fMOST image
579 and the AllenCCFv3 using our pipeline can be applied in this way to fMOST neuron
580 reconstruction data.

581 4.3 Mapping MERFISH data to AllenCCFv3

582 4.3.1 Preprocessing

- 583 • *Initial volume reconstruction.* Alignment of MERFISH data into a 3-D atlas space
584 requires an estimation of anatomical structure within the data. For each section,
585 this anatomic reference image was created by aggregating the number of detected
586 genetic markers (across all probes) within each pixel of a $10 \times 10\mu m^2$ grid to match
587 the resolution of the $10\mu m$ AllenCCFv3 atlas. These reference image sections are then
588 coarsely reoriented and aligned across sections using manual annotations of the most
589 dorsal and ventral points of the midline. The procedure produces an anatomic image
590 stack that serves as an initialization for further global mappings into the AllenCCFv3.
- 591 • *Anatomical correspondence labeling.* Mapping the MERFISH data into the AllenCCFv3
592 requires us to establish correspondence between the anatomy depicted in the MERFISH
593 and AllenCCFv3 data. Intensity-based features in MERFISH data are not sufficiently
594 apparent to establish this correspondence, so we need to generate instead corresponding
595 anatomical labelings of both images with which to drive registration. These labels
596 are already available as part of the AllenCCFv3; thus, the main challenge is deriving
597 analogous labels from the spatial transcriptomic maps of the MERFISH data. Toward
598 this end, we assigned each cell from the scRNA-seq dataset to one of the following major
599 regions: cerebellum, CTXsp, hindbrain, HPF, hypothalamus, isocortex, LSX, midbrain,
600 OLF, PAL, sAMY, STRd, STRv, thalamus and hindbrain. A label map of each section
601 was generated for each region by aggregating the cells assigned to that region within a
602 $10 \times 10\mu m^2$ grid. The same approach was used to generate more fine grained region

603 specific landmarks (i.e., cortical layers, habenula, IC). Unlike the broad labels which
604 cover large swaths of the section these regions are highly specific to certain parts of the
605 section. Once cells in the MERFISH data are labeled, morphological dilation is used to
606 provide full regional labels for alignment into the AllenCCFv3.

- 607 • *Section matching.* Since the MERFISH data is acquired as sections, its 3-D orientation
608 may not be fully accounted for during the volume reconstruction step, due to the
609 particular cutting angle. This can lead to obliqueness artifacts in the section where
610 certain structures can appear to be larger or smaller, or missing outright from the
611 section. To address this, we first use a global alignment to match the orientations of
612 the MERFISH sections to the atlas space. In our pipeline, this section matching is
613 performed in the reverse direction by performing a global affine transformation of the
614 AllenCCFv3 into the MERFISH data space, and then resampling digital sections from
615 the AllenCCFv3 to match each MERFISH section. This approach limits the overall
616 transformation and thus resampling that is applied to the MERFISH data, and, since
617 the AllenCCFv3 is densely sampled, it also reduces in-plane artifacts that result from
618 missing sections or undefined spacing in the MERFISH data.

619 4.3.2 2.5D deformable, landmark-driven alignment to AllenCCFv3

620 After global alignment of the AllenCCFv3 into the MERFISH dataset, 2D per-section
621 deformable refinements are used to address local differences between the MERFISH sections
622 and the resampled AllenCCFv3 sections. Nine registrations were performed in sequence using
623 a single label at each iteration in the following order: 1) brain mask, 2) isocortex (layer
624 2+3), 3) isocortex (layer 5), 4) isocortex (layer 6), 5) striatum, 6) medial habenula, 7) lateral
625 habenula, 8) thalamus, and 9) hippocampus. This ordering was determined empirically by an
626 expert anatomist who prioritized which structure to use in each iteration by evaluating the
627 anatomical alignment from the previous iteration. Global and local mappings are then all
628 concatenated (with appropriate inversions) to create the final mapping between the MERFISH
629 data and AllenCCFv3. This mapping is then used to provide a point-to-point correspondence
630 between the original MERFISH coordinate space and the AllenCCFv3 space, thus allowing

631 mapping of individual genes and cell types located in the MERFISH data to be directly
632 mapped into the AllenCCFv3.

633 4.4 DevCCF velocity flow transformation model

634 Given multiple, linearly or non-linearly ordered point sets where individual points across the
635 sets are in one-to-one correspondence, we developed an approach for generating a velocity
636 flow transformation model to describe a time-varying diffeomorphic mapping as a variant of
637 the landmark matching solution. Integration of the resulting velocity field can then be used
638 to describe the displacement between any two time points within this time-parameterized
639 domain. Regularization of the sparse correspondence between point sets is performed using a
640 generalized B-spline scattered data approximation technique⁴³, also created by the ANTsX
641 developers and contributed to ITK.

642 4.4.1 Velocity field optimization

643 To apply this methodology to the developmental templates¹¹, we coalesced the manual
644 annotations of the developmental templates into 26 common anatomical regions (see Figure
645 3). We then used these regions to generate invertible transformations between successive time
646 points. Specifically each label was used to create a pair of single region images resulting in 26
647 pairs of “source” and “target” images. The multiple image pairs were simultaneously used to
648 iteratively estimate a diffeomorphic pairwise transform. Given the seven atlases E11.5, E13.5,
649 E15.5, E18.5, P4, P14, and P56, this resulted in 6 sets of transforms between successive time
650 points. Approximately 10^6 points were randomly sampled labelwise in the P56 template
651 space and propagated to each successive atlas providing the point sets for constructing the
652 velocity flow model. Approximately 125 iterations resulted in a steady convergence based on
653 the average Euclidean norm between transformed point sets. Ten integration points were
654 used and point sets were distributed along the temporal dimension using a log transform for
655 a more evenly spaced sampling. For additional information a help menu is available for the
656 ANTsPy function `ants.fit_time_varying_transform_to_point_sets(...)`.

657 **4.5 ANTsXNet mouse brain applications**

658 **4.5.1 General notes regarding deep learning training**

659 All network-based approaches described below were implemented and organized in the
660 ANTsXNet libraries comprising Python (ANTsPyNet) and R (ANTsRNet) analogs using the
661 Keras/Tensorflow libraries available as open-source in ANTsX GitHub repositories. For the
662 various applications, both share the identically trained weights for mutual reproducibility.
663 For all GPU training, we used Python scripts for creating custom batch generators which we
664 maintain in a separate GitHub repository for public availability (<https://github.com/ntustison/ANTsXNetTraining>). These scripts provide details such as batch size, choice of loss
666 function, and network parameters. In terms of GPU hardware, all training was done on a
667 DGX (GPUs: 4X Tesla V100, system memory: 256 GB LRDIMM DDR4).

668 Data augmentation is crucial for generalizability and accuracy of the trained networks.
669 Intensity-based data augmentation consisted of randomly added noise (i.e., Gaussian, shot,
670 salt-and-pepper), simulated bias fields based on N4 bias field modeling, and histogram warping
671 for mimicking well-known MRI intensity nonlinearities^{23,46}. These augmentation techniques
672 are available in ANTsXNet (only ANTsPyNet versions are listed with ANTsRNet versions
673 available) and include:

- 674 • image noise: `ants.add_noise_to_image(...)`,
- 675 • simulated bias field: `antspynet.simulate_bias_field(...)`, and
- 676 • nonlinear intensity warping: `antspynet.histogram_warp_image_intensities(...)`.

677 Shape-based data augmentation used both random linear and nonlinear deformations in
678 addition to anisotropic resampling in the three canonical orientations to mimic frequently
679 used acquisition protocols for mice brains:

- 680 • random spatial warping: `antspynet.randomly_transform_image_data(...)` and
- 681 • anisotropic resampling: `ants.resample_image(...)`.

682 **4.5.2 Brain extraction**

683 Similar to human neuroimage processing, brain extraction is a crucial preprocessing step for
684 accurate brain mapping. We developed similar functionality for T2-weighted mouse brains.
685 This network uses a conventional U-net architecture⁴⁷ and, in ANTsPyNet, this functionality is
686 available in the program `antspynet.mouse_brain_extraction(...)`. For the two-shot T2-
687 weighted brain extraction network, two brain templates were generated along with their masks.
688 One of the templates was generated from orthogonal multi-plane, high resolution data³¹ which
689 were combined to synthesize isotropic volumetric data using the B-spline fitting algorithm⁴³.
690 This algorithm is encapsulated in `ants.fit_bspline_object_to_scattered_data(...)`
691 where the input is the set of voxel intensity values and each associated physical location.
692 Since each point can be assigned a confidence weight, we use the normalized gradient value
693 to more heavily weight edge regions. Although both template/mask pairs are available in the
694 GitHub repository associated with this work, the synthesized volumetric B-spline T2-weighted
695 pair is available within ANTsXNet through the calls:

- 696 • template: `antspynet.get_antsxnet_data("bsplineT2MouseTemplate")` and
697 • mask: `antspynet.get_antsxnet_data("bsplineT2MouseTemplateBrainMask")`.

698 **4.5.3 Brain parcellation**

699 The T2-weighted brain parcellation network is also based on a 3-D U-net architecture and
700 the T2-w DevCCF P56 template component with extensive data augmentation, as described
701 previously. Intensity differences between the template and any brain extracted input image
702 are minimized through the use of the rank intensity transform (`ants.rank_intensity(...)`).
703 Shape differences are reduced by the additional preprocessing step of warping the brain
704 extracted input image to the template. Additional input channels include the prior probability
705 images created from the template parcellation. These images are also available through the
706 ANTsXNet `get_antsxnet_data(...)` interface.

707 **Data availability**

708 All data and software used in this work are publicly available. The DevCCF atlas is available
709 at <https://kimlab.io/brain-map/DevCCF/>. ANTsPy, ANTsR, ANTsPyNet, and ANTsRNet
710 are available through GitHub at the ANTsX Ecosystem (<https://github.com/ANTsX>).
711 Training scripts for all deep learning functionality in ANTsXNet can also be found on GitHub
712 (<https://github.com/ntustison/ANTsXNetTraining>). A GitHub repository specifically
713 pertaining to the AllenCCFv3 mapping is available at <https://github.com/dontminchen>
714 [it/CCFAAlignmentToolkit](#). For the other two contributions contained in this work, the interested
715 longitudinal DevCCF mapping and mouse cortical thickness pipeline, we refer the interested
716 reader to <https://github.com/ntustison/ANTsXMouseBrainMapping>.

⁷¹⁷ **Acknowledgments**

⁷¹⁸ Support for the research reported in this work includes funding from the National Institute
⁷¹⁹ of Biomedical Imaging and Bioengineering (R01-EB031722) and National Institute of Mental
⁷²⁰ Health (RF1-MH124605 and U24-MH114827).

⁷²¹ **Author contributions**

⁷²² N.T., M.C., and J.G. wrote the main manuscript text and figures. M.C., M.K., R.D., S.S.,
⁷²³ Q.W., L.G., J.D., C.G., and J.G. developed the Allen registration pipelines. N.T. and F.K.
⁷²⁴ developed the time-varying velocity transformation model for the DevCCF. N.T. and M.T.
⁷²⁵ developed the brain parcellation and cortical thickness methodology. All authors reviewed
⁷²⁶ the manuscript.

727 **References**

- 728 1. Keller, P. J. & Ahrens, M. B. Visualizing whole-brain activity and development at the single-cell level using light-sheet microscopy. *Neuron* **85**, 462–83 (2015).
- 729 2. La Manno, G. *et al.* Molecular architecture of the developing mouse brain. *Nature* **596**, 92–96 (2021).
- 730 3. Wen, L. *et al.* Single-cell technologies: From research to application. *Innovation (Camb)* **3**, 100342 (2022).
- 731 4. Oh, S. W. *et al.* A mesoscale connectome of the mouse brain. *Nature* **508**, 207–14 (2014).
- 732 5. Gong, H. *et al.* Continuously tracing brain-wide long-distance axonal projections in mice at a one-micron voxel resolution. *Neuroimage* **74**, 87–98 (2013).
- 733 6. Li, A. *et al.* Micro-optical sectioning tomography to obtain a high-resolution atlas of the mouse brain. *Science* **330**, 1404–8 (2010).
- 734 7. Ueda, H. R. *et al.* Tissue clearing and its applications in neuroscience. *Nat Rev Neurosci* **21**, 61–79 (2020).
- 735 8. Ståhl, P. L. *et al.* Visualization and analysis of gene expression in tissue sections by spatial transcriptomics. *Science* **353**, 78–82 (2016).
- 736 9. Burgess, D. J. Spatial transcriptomics coming of age. *Nat Rev Genet* **20**, 317 (2019).
- 737 10. Wang, Q. *et al.* The allen mouse brain common coordinate framework: A 3D reference atlas. *Cell* **181**, 936–953.e20 (2020).
- 738 11. Kronman, F. A. *et al.* Developmental mouse brain common coordinate framework. *bioRxiv* (2023) doi:[10.1101/2023.09.14.557789](https://doi.org/10.1101/2023.09.14.557789).
- 739 12. Bajcsy, R. & Broit, C. Matching of deformed images. in *Sixth International Conference on Pattern Recognition (ICPR'82)* 351–353 (1982).
- 740 13. Bajcsy, R. & Kovacic, S. Multiresolution elastic matching. *Computer Vision, Graphics, and Image Processing* **46**, 1–21 (1989).
- 741 14. Gee, J. C., Reivich, M. & Bajcsy, R. Elastically deforming 3D atlas to match anatomical brain images. *J Comput Assist Tomogr* **17**, 225–36 (1993).

- 742 15. Avants, B. B., Epstein, C. L., Grossman, M. & Gee, J. C. [Symmetric diffeomorphic](#)
image registration with cross-correlation: Evaluating automated labeling of elderly
and neurodegenerative brain. *Med Image Anal* **12**, 26–41 (2008).
- 743 16. Klein, A. *et al.* Evaluation of 14 nonlinear deformation algorithms applied to human
brain MRI registration. *Neuroimage* **46**, 786–802 (2009).
- 744 17. Murphy, K. *et al.* Evaluation of registration methods on thoracic CT: The EMPIRE10
challenge. *IEEE Trans Med Imaging* **30**, 1901–20 (2011).
- 745 18. Baheti, B. *et al.* The brain tumor sequence registration challenge: Establishing
correspondence between pre-operative and follow-up MRI scans of diffuse glioma
patients. (2021).
- 746 19. Avants, B. B. *et al.* The optimal template effect in hippocampus studies of diseased
populations. *Neuroimage* **49**, 2457–66 (2010).
- 747 20. Avants, B. B., Tustison, N. J., Wu, J., Cook, P. A. & Gee, J. C. An open source
multivariate framework for n-tissue segmentation with evaluation on public data.
Neuroinformatics **9**, 381–400 (2011).
- 748 21. Manjón, J. V., Coupé, P., Martí-Bonmatí, L., Collins, D. L. & Robles, M. Adaptive
non-local means denoising of MR images with spatially varying noise levels. *J Magn
Reson Imaging* **31**, 192–203 (2010).
- 749 22. Tustison, N. J. *et al.* N4ITK: Improved N3 bias correction. *IEEE Trans Med Imaging*
29, 1310–20 (2010).
- 750 23. Tustison, N. J. *et al.* The ANTsX ecosystem for quantitative biological and medical
imaging. *Sci Rep* **11**, 9068 (2021).
- 751 24. Wang, H. *et al.* Multi-atlas segmentation with joint label fusion. *IEEE Trans Pattern
Anal Mach Intell* **35**, 611–23 (2013).
- 752 25. Tustison, N. J. *et al.* Optimal symmetric multimodal templates and concatenated
random forests for supervised brain tumor segmentation (simplified) with ANTsR.
Neuroinformatics (2014) doi:10.1007/s12021-014-9245-2.

- 753 26. Tustison, N. J., Yang, Y. & Salerno, M. [Advanced normalization tools for cardiac motion correction](#). in *Statistical atlases and computational models of the heart - imaging and modelling challenges* (eds. Camara, O. et al.) vol. 8896 3–12 (Springer International Publishing, 2015).
- 754 27. McCormick, M., Liu, X., Jomier, J., Marion, C. & Ibanez, L. [ITK: Enabling reproducible research and open science](#). *Front Neuroinform* **8**, 13 (2014).
- 755 28. Beg, M. F., Miller, M. I., Trouvé, A. & Younes, L. [Computing large deformation metric mappings via geodesic flows of diffeomorphisms](#). *International Journal of Computer Vision* **61**, 139–157 (2005).
- 756 29. Tustison, N. J. & Avants, B. B. [Explicit B-spline regularization in diffeomorphic image registration](#). *Front Neuroinform* **7**, 39 (2013).
- 757 30. Hsu, L.-M. *et al.* CAMRI mouse brain MRI data.
- 758 31. Reshetnikov, V. *et al.* High-resolution MRI data of brain C57BL/6 and BTBR mice in three different anatomical views.
- 759 32. Rahman, N., Xu, K., Budde, M. D., Brown, A. & Baron, C. A. [A longitudinal microstructural MRI dataset in healthy C57Bl/6 mice at 9.4 tesla](#). *Sci Data* **10**, 94 (2023).
- 760 33. Gong, H. *et al.* [High-throughput dual-colour precision imaging for brain-wide connectome with cytoarchitectonic landmarks at the cellular level](#). *Nat Commun* **7**, 12142 (2016).
- 761 34. Wang, J. *et al.* [Divergent projection patterns revealed by reconstruction of individual neurons in orbitofrontal cortex](#). *Neurosci Bull* **37**, 461–477 (2021).
- 762 35. Rotolo, T., Smallwood, P. M., Williams, J. & Nathans, J. [Genetically-directed, cell type-specific sparse labeling for the analysis of neuronal morphology](#). *PLoS One* **3**, e4099 (2008).
- 763 36. Peng, H. *et al.* [Morphological diversity of single neurons in molecularly defined cell types](#). *Nature* **598**, 174–181 (2021).
- 764 37. Yao, Z. *et al.* [A high-resolution transcriptomic and spatial atlas of cell types in the whole mouse brain](#). *Nature* **624**, 317–332 (2023).

- 765 38. Liu, J. *et al.* Concordance of MERFISH spatial transcriptomics with bulk and
single-cell RNA sequencing. *Life Sci Alliance* **6**, (2023).
- 766 39. Stringer, C., Wang, T., Michaelos, M. & Pachitariu, M. Cellpose: A generalist
algorithm for cellular segmentation. *Nat Methods* **18**, 100–106 (2021).
- 767 40. Das, S. R., Avants, B. B., Grossman, M. & Gee, J. C. Registration based cortical
thickness measurement. *Neuroimage* **45**, 867–79 (2009).
- 768 41. Tustison, N. J. *et al.* Large-scale evaluation of ANTs and FreeSurfer cortical thickness
measurements. *Neuroimage* **99**, 166–79 (2014).
- 769 42. Tustison, N. J. *et al.* Longitudinal mapping of cortical thickness measurements: An
Alzheimer's Disease Neuroimaging Initiative-based evaluation study. *J Alzheimers Dis*
(2019) doi:[10.3233/JAD-190283](https://doi.org/10.3233/JAD-190283).
- 770 43. Tustison, N. J. & Amini, A. A. Biventricular myocardial strains via nonrigid registration
of anatomical NURBS model [corrected]. *IEEE Trans Med Imaging* **25**, 94–112 (2006).
- 771 44. Avants, B. B. *et al.* The Insight ToolKit image registration framework. *Front Neu-
roinform* **8**, 44 (2014).
- 772 45. Avants, B. B. *et al.* A reproducible evaluation of ANTs similarity metric performance
in brain image registration. *Neuroimage* **54**, 2033–44 (2011).
- 773 46. Nyúl, L. G., Udupa, J. K. & Zhang, X. New variants of a method of MRI scale
standardization. *IEEE Trans Med Imaging* **19**, 143–50 (2000).
- 774 47. Falk, T. *et al.* U-net: Deep learning for cell counting, detection, and morphometry.
Nat Methods **16**, 67–70 (2019).